

then, the exhaust from the Explorer's pumped CTD removes settled particles and the transmission counts are read again. The difference between "after" and "before" readings divided by the time that the Explorer was parked at depth gives the CFI (counts/day). More detail, including pictures of instrument setup, is found in (6).

8. The serial numbers of the Explorers are assigned by the Scripps Instrument Development Group; we retain these identities because they uniquely identify the data sets underlying this paper. For simplicity, we refer to Explorer 1177 as the "control" Explorer and Explorer 2104 as the "in-patch" Explorer. Explorers 2054 and 2103 were also deployed "in patch" at 55°S and 66°S, respectively. The POC sensor on Explorer 2054 had a start-up problem that precluded CFI results; poor data transmission success resulted in only sporadic profile data (29 profiles in 2 months). The first week of 2054's profile data is combined with the time series from 2104 in Fig. 2A. Data from 2054 beginning 2 weeks after its deployment no longer showed evidence of the iron-enhanced biomass. Explorers 1177 and 2104 operated for more than 14 months; Explorer 2103, deployed at 66°S, last communicated on 23 July 2003, 18 months after deployment.
9. Retrospective analysis shows that Explorer 2104 was deployed 8 km north of the Monterey Bay Aquarium Research Institute's "center" drifter and near the north edge of the second patch laid down by R/V *Revelle*. In the coordinate system of Explorer 2104, it was deployed approximately 7 km west of the second Fe patch and ~8 km north of the drifter. The float, however, was deployed in waters containing SF6 and immediately registered higher POC levels. During *Revelle*'s second visit to the North Patch in early February 2002, the float was "in" the narrow feature (6).
10. Moderate Resolution Imaging Spectroradiometer (MODIS) satellite image of surface chlorophyll was provided by F. Chavez and is described in (4).
11. Two pairs of Carbon Explorers operating in high-nutrient, low chlorophyll waters of the subarctic North Pacific in 2001 and 2003 yielded virtually identical biomass records over much longer periods (5, 24) and thus provide confidence in the differences described here.
12. Mixed-layer depth is the depth where seawater potential density is increased by 0.05 units relative to the surface value.
13. D. A. Siegel, W. G. Deuser, *Deep-Sea Res.* **44**, 1519 (1997).
14. K. Buesseler, J. Andrews, S. Pike, M. Charrette, *Science* **304**, 414 (2004).
15. Carbon export through 100 m beneath the patch at 66°S was estimated using a one-dimensional Th-234 versus U-238 disequilibrium model (14). Values increased from ~3 (average of "in" and "out" patch day zero values) to 12 mmol C m⁻² d⁻¹ between 24 January and 21 February 2002 (UTC days 24 to 52; patch days 0 to 28). Buesseler *et al.* (14) interpret Th-234-based carbon export estimates as reflecting time scales of "several days to weeks"; thus, a comparison of CFI records averaged over "week" time scales is appropriate. At 66°S, Carbon Explorer 2103's CFI values from 5 to 14 February (UTC days 36 to 45; patch days 12 to 23) averaged 800 counts d⁻¹ (SE = 350 counts d⁻¹; n = 9). Eliminating the first CFI reading yielded an average of 518 counts d⁻¹ (SE = 138 counts d⁻¹; n = 8). The Th-234-based carbon export linearly interpolated to the time of the Explorer data = 9 mmol C m⁻² d⁻¹. CFI of 800 counts d⁻¹ divided by 9 mmol C m⁻² d⁻¹ = 89 counts d⁻¹ (mmol C m⁻² d⁻¹)⁻¹; similarly, the 8-day averaged result = 58 counts d⁻¹ (mmol C m⁻² d⁻¹)⁻¹.
16. S. Honjo, R. Francois, S. Manganini, J. Dymond, R. Collier, *Deep-Sea Res.* **47**, 3521 (2000).
17. J. H. Martin, G. A. Knauer, D. M. Karl, W. W. Broenkow, *Deep-Sea Res.* **34**, 267 (1987).
18. At 55°S, SOFeX Th-234 export estimates were not possible because of sparse ship coverage. Here, we can compare the average of the 2-month control Explorer (1177) CFI values with 1000-m sediment trap results for the same season and location but different year, reported by Honjo *et al.* (17). Carbon-flux estimates from Honjo *et al.* are extrapolated upward to 100 m

using the Martin *et al.* (19) relationship. Depending on which set of three 17-day-long trap samples are used, we get conversion factors ranging from 50 to 80 counts (mmol C m⁻²)⁻¹. Given these similar values but recognizing the uncertainty of calibration, we apply 66°S CFI calibration factors of 58 and 89 counts (mmol C m⁻²)⁻¹ to 55°S CFI data.

19. Standing stocks of POC changed from about 9 to 2 mmol C m⁻³ over the export period. Assuming that the layer originally was ~40 m thick, we get a net loss of POC = 7 mmol m⁻³ × 40 m = 280 mmol C m⁻². POC loss estimated using profile data reported by Coale *et al.* (North patch RV *Revelle* station 32; rosette-collected water samples filtered through Whatman GFF filters) yields a difference of 8.5 mmol m⁻³ × 40 m = 340 mmol C m⁻². These calculations assume no net production of POC over the 2-week period of the loss and thus represent lowest estimates.
20. I. Y. Fung *et al.*, *Global Biogeochem. Cycles* **14**, 281 (2000).
21. J. H. Martin, R. M. Gordon, S. Fitzwater, W. B. Broenkow, *Deep-Sea Res.* **36**, 649 (1989).
22. P. W. Boyd *et al.*, *Nature* **407**, 695 (2000).
23. F. Gervais, U. Riebesell, M. Y. Gorbunov, *Limnol. Oceanogr.* **47**, 1324 (2002).
24. J. K. B. Bishop, unpublished data.

25. We thank K. Johnson and F. Chavez, Moss Landing Marine Laboratories; C. Guay, Lawrence Berkeley National Laboratory (LBNL), and P. Lam, LBNL/University of California, Berkeley; and the crew and scientific parties aboard RV *Revelle* for their assistance. We thank M. Altabet and D. Timothy for their measurements of POC in multiple unit large volume in-situ filtration system (MULVFS) samples and for providing the Rosette POC results described in (6). This work was supported by the U.S. Department of Energy (DOE) Office of Science, Office of Biological and Environmental Research (KP1202030). Implementation of the CFI scheme on DOE SOFeX Explorers was supported through the National Oceanographic Partnership Program (N00014-99-F0450 to LBNL and N00014-99-1-1045 to Scripps Institute of Oceanography).

Supporting Online Material

www.sciencemag.org/cgi/content/full/304/5669/4177
DC1

Materials and Methods

Figs. S1 to S11

References

6 June 2003; accepted 26 February 2004

Vortex Core–Driven Magnetization Dynamics

S.-B. Choe,^{1*} Y. Acremann,² A. Scholl,¹ A. Bauer,^{1,2,3} A. Doran,¹
J. Stöhr,² H. A. Padmore¹

Time-resolved x-ray imaging shows that the magnetization dynamics of a micron-sized pattern containing a ferromagnetic vortex is determined by its handedness, or chirality. The out-of-plane magnetization in the nanometer-scale vortex core induces a three-dimensional handedness in the planar magnetic structure, leading to a precessional motion of the core parallel to a subnanosecond field pulse. The core velocity was an order of magnitude higher than expected from the static susceptibility. These results demonstrate that handedness, already well known to be important in biological systems, plays an important role in the dynamics of microscopic magnets.

Magnetic films of a thickness below the magnetic exchange length form planar magnetic structures. Generally, the magnetization of such films is forced into the sample plane by the magnetic shape anisotropy. An exception to this rule is the magnetic vortex, a magnetic curl that appears at the intersection of Néel walls and in crosstie walls. Recent microscopic experiments have shown—as theory has long predicted—that vortices are three-dimensional structures that possess nanometer-sized cores in which the curling magnetization turns out-of-plane, avoiding the high energetic cost of anti-aligned moments (1, 2). For data storage purposes, magnetic vortices can be trapped in lithographically defined, rectangular or circular magnetic patterns.

They are of considerable technological interest, because the low magnetic stray field leads to a high magnetic stability and minimizes the cross-talk between adjacent vortices—two prerequisites for high integration density. We demonstrate that the out-of-plane magnetization in the nanometer-scale vortex core dominates the nanosecond magnetization dynamics of micron-sized vortex patterns. The observed gyrotropic motion of the vortex core around the pattern center corresponds to a subgigahertz mode seen in micromagnetic simulations and recent magneto-optical experiments (3–6).

Ultrafast techniques generally use pulsed optical lasers in a pump-probe arrangement (7, 8). Although very high time resolution can be achieved, the spatial resolution of optical experiments is diffraction-limited by the wavelength of light to ~400 nm. This limitation can be overcome by x-ray imaging techniques. X-ray magnetic circular and linear dichroism (XMCD and XMLD) at the transition metal L edges probe the direction and size of the element-specific magnetic

¹Lawrence Berkeley National Laboratory (LBNL), 1 Cyclotron Road, Berkeley, CA 94720, USA. ²Stanford Synchrotron Radiation Laboratory, Post Office Box 20450, Stanford, CA 94309, USA. ³Freie Universität Berlin, Arnimallee 14, D-14195 Berlin, Germany.

*To whom correspondence should be addressed. E-mail: SBChoe@lbl.gov

moment. They have been successfully used for high-resolution magnetic domain imaging with photoemission electron microscopes (PEEMs) (9, 10). We used the PEEM-2 microscope at the Advanced Light Source, which reaches a spatial resolution of well below 100 nm. The duration of the x-ray pulse, ~ 70 ps, sets the time resolution (11).

About 40 magnetic structures of different sizes and shapes were patterned by focused ion beam into a 20-nm-thick, magnetically soft CoFe alloy film on top of a Cu waveguide. Fast in-plane magnetic field pulses were derived from 300-ps [full width at half maximum (FWHM)] current pulses, launched in a GaAs photoconductive switch. We focused our analysis on four rectangular structures, each of which contained a single trapped vortex at the intersection of two diagonal Néel walls. Magnetic domain images of the in-plane magnetization of these structures, sized $1 \times 1 \mu\text{m}^2$ (I), $1.5 \times 1 \mu\text{m}^2$ (II and III), and $2 \times 1 \mu\text{m}^2$ (IV), are shown in Fig. 1. The images were computed as the ratio of two PEEM images acquired at the Co L_3 and L_2 absorption resonances. Cross-correlation of gradient images was used to trace the position of the vortex center as a function of time (Fig. 1, bottom). The center position was determined with a precision beyond the intrinsic resolution of PEEM because of the strong magnetic contrast and low image noise.

We observed two phases of vortex dynamics: an initial linear acceleration in response to the field pulse, followed by a gyrotropic rotation driven by the in-plane magnetostatic field of the excited vortex. The curling orientation of the in-plane domain structure was not correlated with the direction of the initial acceleration or the rotation sense of the gyrotropic mode. For example, patterns II and III have similar in-plane magnetic structures but show opposite accelerations and gyrotropic motions. Patterns I and IV have oppositely oriented in-plane magnetic structures but show the same gyrotropic motions. A hidden parameter is present that rules the subnanosecond dynamical response of a vortex. This hidden parameter is the direction of the out-of-plane magnetization of the core, which is invisible in this experiment and induces a three-dimensional handedness, or chirality, in the vortex.

Figure 2A illustrates the spin structure of left-handed and right-handed square vortices (1, 2). Intuitively, one expects an external magnetic field H to result in the growth of domain 4, which is aligned with the field, and to lead, consequently, to a transverse motion of the vortex center. Experimentally, however, we observed an initial motion along the field direction during the fast, subnanosecond field pulse (Fig. 1) (12). The vortex center moves parallel to

the field because, on a subnanosecond time scale, magnetic moment precession around the field direction dominates over damping in the field direction. When viewed along the direction of the external field H , the magnetic moments in left- and right-handed vortex structures experience a clockwise precessional torque about the H direction (Fig. 2, blue arrows). In a left-handed vortex, the magnetization in domain 3 precesses in the direction of the core magnetization, which itself precesses in the direction of the magnetization in domain 1. This corresponds to a motion of the vortex core antiparallel to the applied field. In contrast, for a right-handed vortex, the magnetization in domain 1 precesses in the

direction of the core magnetization, resulting in a parallel motion. The vortex handedness (shown in Figs. 1 and 2) thus controls the fast, precessional dynamics of a micron-scale vortex pattern.

The displacement of the core after the field pulse powers the gyrotropic motion of the vortex. The imbalance of the in-plane magnetization creates a magnetostatic field perpendicular to the displacement, which drives the vortex on a spiraling trajectory. For all vortices, the sense of the gyrotropic motion is counterclockwise when the direction of the out-of-plane magnetization at the core points toward the viewer. Although this result may at first seem surprising, it is in fact a simple consequence of the definition of

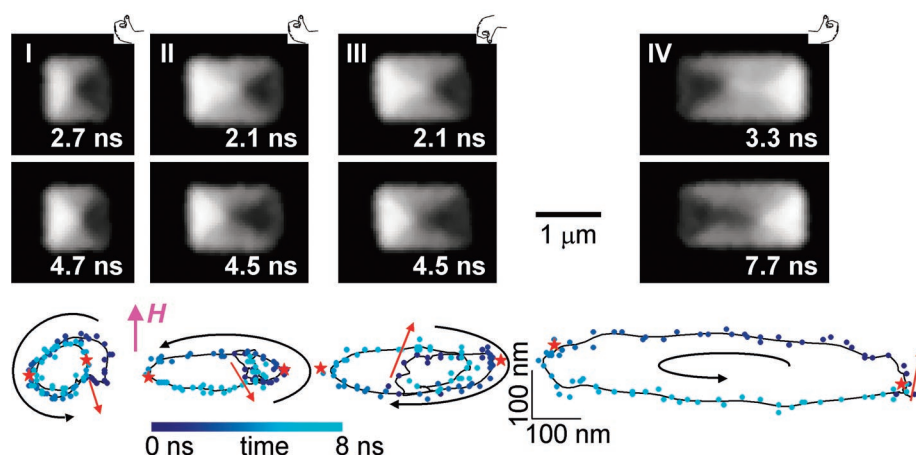
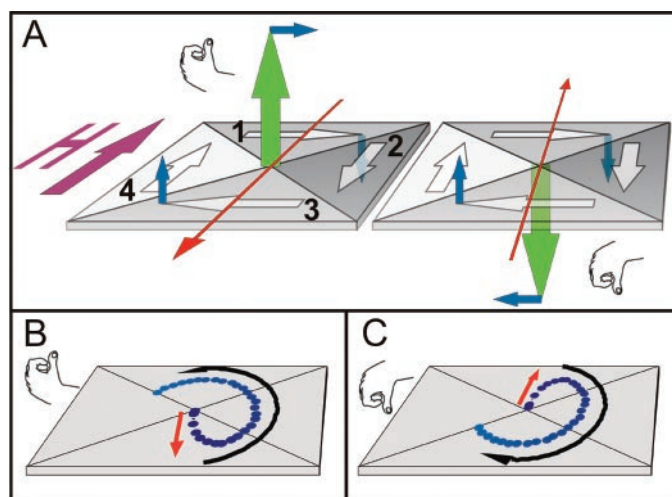


Fig. 1. (Top) Domain images of the in-plane magnetization of Pattern I ($1 \times 1 \mu\text{m}^2$), Patterns II and III ($1.5 \times 1 \mu\text{m}^2$), and Pattern IV ($2 \times 1 \mu\text{m}^2$), taken at the specified delay times after the field pulse. The images are part of a time series that extends over 8 ns and were chosen so that the horizontal displacement of the vortex has maximum amplitude. Hands illustrate the vortex handedness and the out-of-plane core magnetization as determined from the vortex dynamics. **(Bottom)** Trajectories of the vortex core. The dots represent sequential vortex positions (in 100-ps steps). Lines represent time-averaged positions with a Gaussian weight function of 100 ps (FWHM) for 0 to 1 ns and 400 ps (FWHM) for 1 to 8 ns. The progression in time is symbolized by the dot color. Red arrows show the trajectory during the field pulse; black arrows show the direction of gyrotropic rotation after the pulse; and red stars show the vortex position for the shown domain images.

Fig. 2. (A) Spin structure (white arrows) of a left-handed (left side) and a right-handed (right side) square vortex. Blue arrows represent the precessional torque generated by the external magnetic field (purple arrow). Hands illustrate the vortex handedness, and a green arrow indicates the out-of-plane core magnetization. Red arrows indicate the acceleration direction in response to the field. **(B and C)** Simulated trajectory of the core of (B) a left-handed and (C) a right-handed vortex during and after a field pulse.



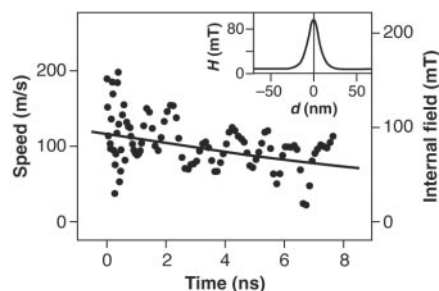


Fig. 3. Vortex speed with respect to the delay time after the field pulse (black dots). The speed was computed from the time-averaged core positions of Pattern I. The solid line is a fit with an exponential function showing a decline in speed, which is the result of damping. The inset shows the simulated profile of the internal field along a cut through the vortex core parallel to the direction of motion.

magnetic fields and moments in a right-handed coordinate system. It does not imply a broken parity. Micromagnetic simulations of the core motion during the first 3 ns are shown in Fig. 2 (B and C) (13). During the external field pulse, the core moves either parallel or antiparallel to the field, depending on the vortex handedness. Afterward, the trajectory turns parallel or antiparallel to the magnetostatic field and the core starts its gyrotropic motion, in agreement with the experiment.

A first estimate of the field H that is driving the vortex motion can be made with the vortex susceptibility χ , which relates the in-plane magnetization density m_d to the field H for a given displacement of the core d , according to $\chi H = m_d = d/l \cdot M_s$. The magnetization density is a linear function of the displacement d , where M_s is the saturation magnetization. We considered a square vortex of length $l = 1 \mu\text{m}$, for which the vortex susceptibility has been determined by simulations to be $\sim 4 \times 10^5$ henries per meter in agreement with experiments (14). For the observed vortex displacement $d = 50 \text{ nm}$, the resulting average internal field is $H = 3 \text{ mT}$. Assuming that this field powers the gyrotropic motion of the vortex center, the speed V of the core can be estimated using $V \approx 2\gamma bH/\pi$. This formula reflects that the precession of core spins by $\pi/2$ corresponds to the translation of the core by its diameter b . γ is the gyromagnetic ratio. Therefore, using $b = 10 \text{ nm}$ (15), we expected a vortex speed of $\sim 4 \text{ m/s}$. However, the experimentally determined vortex speed after the field pulse was close to 100 m/s (Fig. 3). This leads us to the conclusion that the internal field near the core must be considerably higher than the average field estimated with the static susceptibility. By inverting $V \approx 2\gamma bH/\pi$, we translated the measured vortex speed into an experimentally determined local field at the core (Fig. 3, right axis). The size of this

field, $\sim 80 \text{ mT}$, is in good quantitative agreement with the result of a micromagnetic simulation (Fig. 3, inset) (13). The field profile shows a considerably enhanced value at the core that rapidly decreases with increasing distance. This enhanced core field is a consequence of the deformation of the magnetic structure of the vortex core during its gyrotropic motion. Thus, both direction and speed of the nanosecond magnetization dynamics of a vortex are determined by the peculiar structure of the nanometer-scale core.

Accurate measurement of the position and speed of the vortex center thus provides information about the local magnetic fields and the resulting torques in a magnetic pattern on a nanometer scale. The study of picosecond magnetization dynamics on this scale will provide fundamental insight into the properties of mesoscopic magnetic structures, which are the fundamental building blocks of magnetoelectronic devices.

References and Notes

1. T. Shinjo, T. Okuno, R. Hassdorf, K. Shigeto, T. Ono, *Science* **289**, 930 (2000).
2. A. Wachowiak *et al.*, *Science* **298**, 577 (2002).
3. B. E. Argyle, E. Terrenzio, J. C. Slonczewski, *Phys. Rev. Lett.* **53**, 190 (1984).
4. A. R. Volkel, G. M. Wysin, F. G. Mertens, A. R. Bishop, H. J. Schnitzer, *Phys. Rev. B* **50**, 12711 (1994).
5. K. Yu. Guslienko *et al.*, *J. Appl. Phys.* **91**, 8037 (2002).

6. J. P. Park, P. Eames, D. M. Engebretson, J. Berezovsky, P. A. Crowell, *Phys. Rev. B* **67**, 020403 (2003).
7. Y. Acremann *et al.*, *Science* **290**, 492 (2000).
8. Th. Gerrits, H. A. M. van den Berg, J. Hohlfield, K. Bär, Th. Rasing, *Nature* **418**, 509 (2002).
9. J. Stöhr *et al.*, *Science* **259**, 658 (1993).
10. A. Scholl *et al.*, *Science* **287**, 1014 (2000).
11. Materials and methods are available as supporting material on Science Online.
12. A gyrotropic motion in the magnetostatic field of the displaced vortex is superimposed, explaining the angle of the initial acceleration to the external field.
13. Simulations were performed on 20-nm-thick, $1 \times 1 \mu\text{m}^2$ squares divided into 3.3-nm square cells. We used a saturation magnetization of 1.88 T, an exchange stiffness of $3.0 \times 10^{-11} \text{ J/m}$, no crystalline anisotropy, and a damping constant of 0.02.
14. M. Natali *et al.*, *Phys. Rev. Lett.* **88**, 157203 (2002).
15. $b = 2\sqrt{2A/\mu_0 M_s^2}$ approximates core diameter with exchange stiffness A (2).
16. We thank the National Center for Electron Microscopy LBNL and the Microlab at the University of California-Berkeley for giving us access to their lithography facilities and H. C. Siegmann for many valuable discussions. Supported by the Office of Basic Energy Sciences of the U.S. Department of Energy (A.L.S. and S.S.R.L.), by the Laboratory Directed Research and Development Program of LBNL, and by the National Science Foundation under grant no. DMR-0203835 (J.S.).

Supporting Online Material

www.sciencemag.org/cgi/content/full/304/5669/420/DC1

Materials and Methods
Figs. S1 and S2
Movie S1

23 December 2003; accepted 5 March 2004

Ultrahigh Strength and High Electrical Conductivity in Copper

Lei Lu, Yongfeng Shen, Xianhua Chen, Lihua Qian, K. Lu*

Methods used to strengthen metals generally also cause a pronounced decrease in electrical conductivity, so that a tradeoff must be made between conductivity and mechanical strength. We synthesized pure copper samples with a high density of nanoscale growth twins. They showed a tensile strength about 10 times higher than that of conventional coarse-grained copper, while retaining an electrical conductivity comparable to that of pure copper. The ultrahigh strength originates from the effective blockage of dislocation motion by numerous coherent twin boundaries that possess an extremely low electrical resistivity, which is not the case for other types of grain boundaries.

For conducting materials in many applications, high electrical conductivity and high mechanical strength are often required simultaneously. However, pure metals with high conductivities such as Ag, Cu, and Al are very soft. Strengthening the metals via various approaches, including solid solution alloying, cold working, and grain refinement, leads to a pronounced decrease in conductivity.

For example, alloying pure Cu may increase the strength by two or three times, but the electrical conductivity of Cu alloys is only 10 to 40% that of pure Cu (1).

The strength of a solid is determined by the solid's resistance to plastic deformation, and it is sensitive to the solid's chemical composition and microstructure. Plastic deformation of conventional polycrystalline metals is mainly carried by lattice dislocations within individual grains. Several strengthening methodologies have been developed to restrict the dislocation motion. For example, refining grains introduces more grain boundaries (GBs), which are barriers to

Shenyang National Laboratory for Materials Science (SYNL), Institute of Metal Research, Chinese Academy of Sciences, Shenyang 110016, P.R. China.

*To whom correspondence should be addressed. E-mail: lu@imr.ac.cn